SEISMIC MELTWATER RESPONSE FROM BLOOD FALLS, TAYLOR GLACIER, ANTARCTICA

JOSHUA D CARMICHAEL, ERIN PETTIT, MATT HOFFMAN, BERNARD HALLET, ANDREW FOUNTAIN

Abstract. Meltwater input often triggers a seismic response from glaciers and ice sheets. It is difficult to measure melt production on glaciers directly, however, while subglacial water storage is inherently not observable. Therefore, we perform a meltwater sensitivity test of a dry-based polar glacier (Taylor Glacier, Antarctica) during a summer season using a synthesis of melt modeling and seismic observation. We estimate melt input with a calibrated surface energy balance model and measure the response using array-based analyses of icequakes recorded at a small aperture seismic array. In the absence of modeled surface melt, we find that seismicity is well-described by a diurnal signal composed of numerous small icequakes. During melt events, the diurnal signal is suppressed and seismicity is instead characterized by large glacial icequakes. We perform array-based correlation and clustering analyses and determine that a large percentage of melt-season icequakes are repeating events (multiplets). The epicentral locations for these multiplets suggest that they are triggered by meltwater produced near a brine seep known as Blood Falls. Our observations of the corresponding p-wave first motions are consistent with volumetric source mechanisms. We suggest that surface melt enables a persistent pathway through this cold ice to an englacial fracture system that is responsible for brine release episodes from Blood Falls crack system. The scalar moment for these events suggest that the volumetric increase at the source region can be explained by melt input alone.

1. Introduction

Seismic observation of glaciers and ice-sheets provide a high sample-rate coverage of elastic ice deformation that cannot be obtained with other instrumentation. Seismic arrays provide improved detection thresholds over single seismometers and the necessary spatial coverage for performing inversion of observables such as icequake hypocenters and focal mechanisms. In particular, seismic monitoring have been successfully used in the detection and interpretation of melt-triggered ice-quakes. Meltwater has been deduced to trigger glacial faulting [Walter et al., 2010], basal stick-slip sliding [Weaver and Malone, 1979], and rapid fracture events [Roux et al., 2010, Das et al., 2008] that release microseismic energy. However, direct observations of melt generation are difficult to acquire. Challenges include quantifying firn storage capacity [Clarke, 2005], subsurface melting [Liston et al., 1999], and discriminating between ablation and surface melt [Hoffman, 2011]. We suggest that improved confidence in the production of meltwater is necessary to bound the influence it has on ice deformation. We therefore study a glacial regime in which no firn is present, meltwater can be confidently modeled, and seismic monitoring is available to estimate icequake characteristics.

2. Background

The deformation processes that require persistent englacial water and produce seismic emissions in temperate glaciers may not be present in cold glaciers. Our interest here is to determine which processes are most responsive to the introduction of water by interpreting icequake emissions from a polar glacier during a brief melt season. We propose that it is necessary to study a setting where water availability and basal sliding are initially absent, and subsequent surface melt can be adequately estimated. The melt-induced seismic response of the glacier from dry initial conditions will then provide a sensitivity test of exposure to surface melt. This test would address two primary questions: First, "over what time scale does a glacier respond to surface melt?", and second "what deformation mechanisms, if any, are first initiated by surface melt?'

To confront these questions we consider Taylor Glacier, a polar glacier in the McMurdo Dry Valleys of Antarctica, during a typical melt season (Figure 1). The mean annual and summer temperatures (respectively -17°C, -3°C, [Hoffman et al., 2008]) are consistent with a cold environment with limited meltwater input that we require for a study site. Previous work near the Taylor terminus includes analyses of surface energy balance [Hoffman et al., 2008,

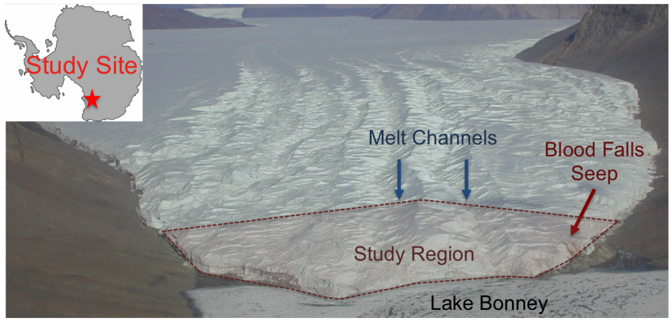

FIGURE 1. *Taylor Glacier ($77°44'$ S, $162°10'$ E) is an outlet from the East Antarctic Ice Sheet that terminates at the shore of perennially frozen Lake Bonney in the western side of Taylor Valley. The shaded region approximates the study area. View here is looking East of the terminus (Photo: Thomas Nylen).*

Johnston et al., 2005], and the geochemistry of an iron-brine discharge from a stationary seep known as Blood Falls [Mikucki et al., 2009]. For our purposes the energy balance provides a means to estimate surface melt production, and the seep of Blood Falls is important as a surface-to-englacial pathway for meltwater. In this paper, we present evidence that even very small melt rates on polar glaciers ($\leq 1.2\,\mathrm{mm\,hr^{-1}}$) produce a response that is qualitatively distinct from melt-free conditions, and may trigger relatively large englacial fracture events where liquid water was not expected to exist. Our results follow from a novel array-based processing methodology that we have developed for detection of repeating icequakes and describe here.

2.1. **Study Area.** Glaciers in the McMurdo Dry Valleys are representative of cold-based polar glaciers due to the ice-free polar desert environment they occupy [Fountain et al., 2006]. Among these is Taylor Glacier, which enters Taylor Valley as an outlet from the East Antarctic Ice sheet and terminates at the western lobe of the perennially ice-covered Lake Bonney (Figure 1). Prominent features of the glacier include a pair of meltwater channels that form 7 km upstream and deepen along flow, reaching a depth of ~ 25 m near the terminus. During the summer months, micro-climatic conditions within these channels favor melt over sublimation, and cause supraglacial water flow [Johnston et al., 2005]. Observed melt is also produced from calving ice cliffs $20-35$ m high at the ablation zone terminus. However, no prior published work indicates that surface melt penetrates to the bottom of Taylor Glacier. Basal ice temperatures recorded near the terminus ($-17°$C) suggest that Taylor is frozen to its substrate, and most of its motion is accommodated by internal creep in the ice and a debris-rich basal ice layer a few meters above the bedrock [Samyn and Fitzsimons, 2008]. A force balance conducted several kilometers up glacier [Kavanaugh and Cuffey, 2009] further suggests that no basal motion is required to explain surface speeds. Taylor Glacier is also the site of Blood Falls, an anomalous iron-rich seep that flows episodically from the northern end of the terminus [Mikucki et al., 2009]. Despite ice flow rates of $3-5\,\mathrm{ma^{-1}}$ the seep location has remained stationary with respect to bedrock, emerging from a set of long cracks. The primary crack present during December 2006 was surveyed with GPS (Thomas Nylen, personal communication) and measured ~ 80 m in extent, with strike $\cong 45°$ East of North. The maximum crack depth is unknown, but exceeds 15 m at some locations, with the crack faces separated by distances of less than 6 m. Other surface cracks upstream of the primary crack run approximately parallel to it and catch summer melt that refreezes as blue ice. The brine emerges near the primary crack as an artesian well, indicating that the fluid is under pressure at depth.

2.2. **Data Collection.** The data were collected using a PASSCAL-supplied seismic array, three UNAVCO-supplied GPS receivers, time-lapsed cameras, and a meteorological station (Figure 2). The cameras were mounted on the valley floor and recorded daily images of the northern ice cliffs from early December 2005 through late March 2006 to document calving events. The meteorological station ($77°42'$S,$162°8'$E) recorded 15 min averages of meteorological conditions that provide the data for surface energy-balance modeling [Hoffman, 2011]. Two continuous GPS stations were deployed on the ice, and a base station was deployed on a nearby benchmark during the summer. Data were collected at 30 sec sample rates during the summer for 24 hr per day, which was reduced to 1 hr during winter. The seismic array was deployed at the terminus region of Taylor Glacier in $2004-2006$. The data acquisition system

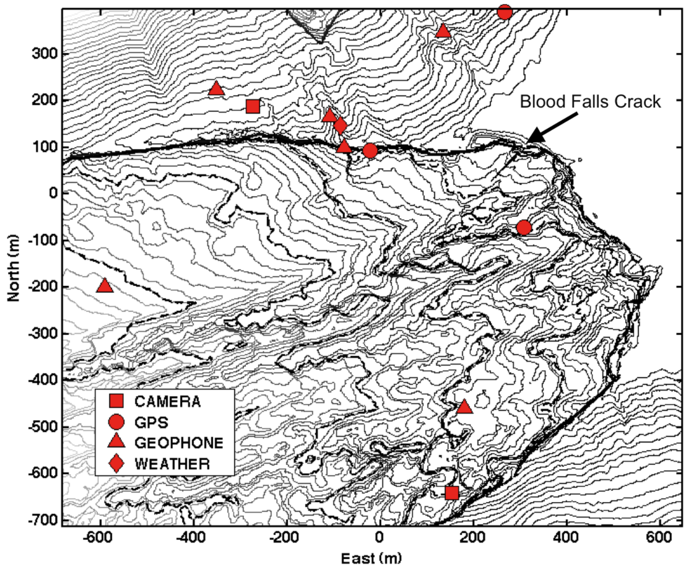

FIGURE 2. *Taylor Glacier instrumentation consisted of a* 6*-receiver,* 3*-component seismic array,* 3 *GPS receivers, weather station, and a time-lapsed camera. The primary Blood Falls crack is labeled for reference. The seismic array operated continuously from* $2004-2006$*. Heavy contour spacing on glacial surface is* 25 meters *(dashed lines).*

(DAS) consisted of six triaxial L-28 geophones equipped with Quanterra Q330 digitizers and solid state data loggers. Ground velocity was sampled at 200 Hz in continuous recording mode and stored on the data loggers, which were retrieved in November, 2006. We deconvolved the cumulative instrument response from these data to recover seismic displacement using a 10^{-10} m water level regularization. Because these DAS time tag data to compensate for linear phase shifts caused by FIR filters [Inc, 2010, Appendix C], we found no need to correct for the acausality of the anti-alaising filter as described elsewhere [Deichmann et al., 2000].

3. Methodology

Our methodology consists of comparing meltwater produced from Taylor Glacier with several measures of microseismic activity. To estimate meltwater production, we use a surface energy balance model (Section 3.1). To process the seismic data, we count events (Section 3.2), cluster seismic record sections (Section 3.3), invert for icequake hypocenters (Section 3.4), and estimate scalar moment of icequakes (Section 3.5).

3.1. **Estimating Surface Melt Production.** It is difficult to measure surface meltwater production on glaciers directly. Total ablation can be measured over finite time periods, e.g. using ablation stakes, but this method includes contributions from both sublimation and melt. Although melt composes the majority of ablation on temperate glaciers, sublimation is a substantial fraction of ablation on Taylor Glacier [Johnston et al., 2005, Hoffman et al., 2008]. This makes ablation-stake measurements of melt inaccurate. Furthermore, melt can occur below the surface in the upper 50 cm through solar heating of the ice while the ice surface remains frozen, a process which cannot be detected with traditional ablation measurements [Hoffman, 2011]. Therefore, to estimate meltwater production from the surface of Taylor Glacier, we use a one-dimensional surface energy balance model that has been calibrated against ablation measurements and tested using ice temperature measurements in the upper meter [Hoffman et al., 2008, Liston et al., 1999]. The surface energy available for melt is computed as the residual from balances between net shortwave radiation, net longwave radiation, the turbulent heat fluxes of sensible and latent heat, and heat conducted into or out of the glacier. This surface energy balance is coupled with a one-dimensional heat transfer equation that is used to calculate the heat flux through the glacier surface and includes a source term for solar radiation absorbed beneath the surface. The distribution of solar radiation with depth is determined by a spectrally-dependent extinction coefficient which is a function of the solar spectrum, ice surface albedo, ice density, and effective ice grain radius [Brandt and Warren, 1993, Liston et al., 1999]. The model's adjustable parameters include the aerodynamic surface roughness (which affects the magnitude of the turbulent heat fluxes, and therefore sublimation), the effective ice grain radius (which determines the distribution of net solar radiation with depth), and the thickness of the surface layer (which determines the fraction of net radiation included in the surface energy balance).

We apply the model using an hourly time step with meteorological forcings of air temperature, relative humidity, wind speed, incoming solar radiation, surface albedo, incoming longwave radiation, and atmospheric pressure. Model outputs at the surface include ice surface temperature and the ablation components of sublimation and melt, and model outputs for the subsurface ice column include temperature, melt flux, and water fraction. The model is applied at a point (162.237°E, 77.726°S) and calibrated to 14 years of summer ablation measurements averaged from three ablation stakes located within 0.5 km [Fountain et al., 2006]. We consider this location representative of the near horizontal surface of the terminal 2 km of Taylor Glacier, exclusive of the large channels and ice cliffs, which have substantially higher melt rates [Johnston et al., 2005], and Blood Falls, which has substantially lower surface albedo and likely higher melt rates. Local meteorological forcings are obtained by applying the quasi-physically based meteorological distribution model MicroMet [Liston and Elder, 2006] from observations at Taylor Glacier and Lake Bonney meteorological stations. The calibration at this location yielded an aerodynamic surface roughness of 0.2 mm, effective ice grain radius of 0.08 mm, and surface layer thickness of 1 cm, comparable to those at the Taylor Glacier meteorological station, 2 km upglacier [Hoffman et al., 2008]. We perform a visual test on surface melt production using the daily images obtained from the time-lapse camera system. During days surface melt occurs in the model, water is visible as a stream around the perimeter of the ice cliffs and diminishes during days modeled melt is absent. We therefore consider the model qualitatively representative of conditions near the ice cliffs as well. The time evolution of predicted melt is illustrated Figure 6 (bottom).

3.2. **Quantifying Seismicity.** To compare our estimates of meltwater production with the emission rate of icequakes (seismicity), we establish a criteria for counting icequakes that is based upon their observability. We first identify seismic events on each station using a standard STA/LTA detection methodology [Roux et al., 2008] in which we compute the ratio between a short-term average (0.5 sec) and long-term average (2.5 sec) of the squared-ground velocity. When this STA/LTA ratio exceeds a threshold of 3.2, we declare a seismic event and retain a 10 second window centered on the pick time to prevent redundant event detections. We chose these picking parameters based upon visual inspection and manual picking of a subset of the data.

To count these events, we define a weighted scoring method that assigns a scalar to each seismic event according to its size, as determined by its detectability at each receiver. A large event should produce observable ground motion at each receiver and closely timed picks, whereas a small event might only be observable by a pair of receivers near the source. If the pick time difference between any pair of receivers is less than or equal to the expected s-wave travel time Δt, we assign the event a count score $C \leq 1$ that depends upon the square-distance between those receivers. This agrees with empirical relationships between detectability and square-distance observed elsewhere [Kijko and Sciocatti, 1995]. Quantitatively, we define this count score using:

$$C(\Delta t) = \sum_{k,n=1}^{N} w_{kn} I_{kn} = \frac{\sum_{k,n=1}^{N} ||\mathbf{r}_k - \mathbf{r}_n||^2 \, I_{kn}}{\sum_{k,n=1}^{N} ||\mathbf{r}_k - \mathbf{r}_n||^2}, \qquad \beta \Delta t \leqq ||\mathbf{r}_k - \mathbf{r}_n|| \,. \tag{1}$$

Here $\mathbf{r}_j$ is the position of receiver j, β is the s-wave speed in ice, and I_{kn} is the indicator function that is one if receivers k and n both detect an event within Δt, and zero otherwise. The weight function w_{kn} is illustrated with it's dependence on array geometry in Figure 3. Events observed at every receiver are given a maximum count score of one, and events observed at only one receiver are discarded. For an N receiver array, this scoring provides $2^N - (N + 1)$ possible combinations of receivers and event size (bins). The events included in each bin are unique, so events are not redundantly counted. We assign each event in the observation period a value $C(\Delta t)$ and sum these count scores in hourly averages to obtain a time series of seismicity. Figure 4 (bottom) illustrates the hourly sum, Figure 5 (left) the amplitude spectra, and Figure 6 the seismicity observed at three sub-arrays compared with modeled surface melt.

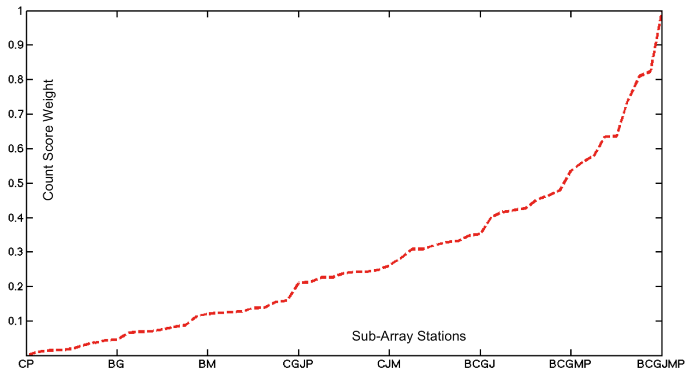

FIGURE 3. *The dependence of weight function w_{kn} (Equation 1) on receiver combination (sub-array) geometry. The horizontal tick-labels give the first initials of each sub-array. For the Blood Falls array,* $10^{-3} \leq w_{kn} \leq 1$.

3.3. **Multiplet Event Detection and Clustering.** Multiplets are distinct, repeating seismic events that produce nearly identical records of ground motion. They provide an observation of repeated stress release from the same source region and from similar source mechanisms [Harris, 1991]. To quantify the similarity between multiplet icequake waveforms, we implement an array-based measure for correlation between events that uses ground motion recorded by all receivers simultaneously. This approach simultaneously improves multiplet detection threshold, while reducing the probability of false multiplet identification [Harris, 2006a, Gibbons and Ringdal, 2006]. A sample of ground motion $\mathbf{u}(t)$ from an N-receiver array is provided by a $3N$ channel record section that we define as:

$$\mathbf{u}(t) = \begin{bmatrix} u_{1e}(t) & u_{1n}(t) & u_{1z}(t) & u_{2e}(t) & u_{2n}(t) & u_{2z}(t) & \ldots & u_{Nz}(t) \end{bmatrix} \quad t \in T. \tag{2}$$

Here $u_{kl}(t)$ symbolizes the ground motion for receiver k in geographical direction l, sampled over time window T. In practice these are samples of ground motion recorded over T seconds, arranged as $3N$ column vectors in a matrix, e.g., $u_{kl}(t) = \mathrm{col}\,[u(t_0), u(t_1) \cdots, u(t_N)]$. If $\mathbf{u}(t)$ and $\mathbf{v}(t)$ are each distinct T second record sections observed at the array, we define their normalized cross correlation to be:

$$\rho \triangleq \max_{\tau} \frac{\langle \mathbf{u}(t), \mathbf{v}(t+\tau) \rangle}{||\mathbf{u}(t)||\,||\mathbf{v}(t)||} = \max_{\tau} \frac{\langle \mathbf{u}(t), \mathbf{v}(t+\tau) \rangle_F}{||\mathbf{u}(t)||_F\,||\mathbf{v}(t)||_F}, \quad -T \leq 2\tau < T \tag{3}$$

Equation 3 assigns a functional on a product space [Stark and Yang, 1998, p. 78], where $\langle \bullet, \bullet \rangle_F$ and $||\bullet||_F$ respectively denote the Frobenius inner product and norm. ρ is bounded by ± 1 and is equivalent to the mean channel correlation. If two sources are separated in distance but are otherwise identical, the differential arrival times between the N receivers cause misalignment between the record sections $\mathbf{u}(t)$ and $\mathbf{v}(t)$ so that $|\rho| < 1$. Thus, ρ near $+1$ requires similar waveforms and source locations, but does not require intra-receiver coherence [Gibbons and Ringdal, 2006]. Quantitative bounds on the cross-correlation between two neighboring sources are given elsewhere [Snieder and Vrijlandt, 2005].

To detect multiplets, we design an unsupervised, partition-based clustering algorithm that groups similar record sections using Equation 3. This algorithm operates in two stages. First, it identifies multiplets from icequake detections during a selected observation period (stage 1), and then builds template waveforms from these multiplets to search the entire observation period for additional events (stage 2). In stage 1, a group of two or more record sections is assigned to a set S (cluster) if the correlation between every possible pair of record sections within S and that group exceeds a threshold of $\rho_0 = 0.65$. We chose this value to reduce false-match probabilities, as determined from Monte-Carlo simulations of cross-correlated noise processes [Harris, 1989]. Because high correlation requires similar source mechanisms and hypocenters, the cluster sets S are therefore populated with record sections that come from multiplet events. The record sections within each cluster S are then coherently aligned (to subsample precision) and stacked to form record section templates. In stage 2, each template is correlated with all other record sections in the catalog. Additional record sections are then added to the pre-exising clusters if they correlates above $\rho_0 = 0.65$ with a template. During both stages, ρ is computed in the frequency domain to sub-sample precision using the

Fourier shifting-property. Stage 1 of our algorithm differs from subspace detectors [Harris, 2006b] in that cluster elements are effectively synthesized from record sections as convex (rather than linear) combinations. Stage 2 of our method differs from other clustering algorithms (e.g., [Thelen et al., 2010]) in two important respects. First, we treat record sections as signals rather than single waveforms; second, the templates are built automatically from mutually correlated sets, so no observer bias is introduced through manual template selection. We provide quantitative details of our methodology in the Appendix.

3.4. **Icequake Hypocentral Inversion.** To estimate hypocenters (source locations) for seismic events, we minimize the error between observed seismic wave arrival times and those computed using a geophysical model. We first estimate waveform arrival times by manually picking phases for a subset of maximum count-score events ($C(\Delta t) = 1$). Waveforms which we include in our phase-picking procedure are constrained in two respects. First, the amplitude and energy of the waveform data limit the number of events for which we can pick first arrivals within acceptable certainty above channel noise. Second, we do not pick first arrivals for those events that give sources exterior to the glacial ice, as determined by the relative order that the p-wave is first observed at the receivers. This quality control removes all but $\cong 150$ events recorded during the melt season between mid December and mid January. From these, we manually select the p-wave and s-wave arrival times, their polarity, and the coda wave duration time for each waveform.

To construct a velocity model of the terminus region of Taylor Glacier, we use a publicly available 2 m resolution DEM (`http://usarc.usgs.gov/lidar_dload.shtml`) and manually digitized the terminus outline. Our velocity model uses seismic wave speeds of $3850\,\mathrm{m\,sec^{-1}}$ for p-waves, $1950\,\mathrm{m\,sec^{-1}}$ for s-waves in the glacier ice and $4800\,\mathrm{m\,sec^{-1}}$ for p-waves, $2900\,\mathrm{m\,sec^{-1}}$ for s-waves in the valley substrate, based partially upon a seismic survey conducted in Beacon Valley [Shean et al., 2007]. Because precise bed topography information is unavailable, the forward model is effectively two-dimensional and does not include vertical velocity gradients as would be present at the ice-bedrock interface.

To produce each hypocenter estimate, we first perform a search over a 2-D grid to find an epicentral grid point 30 m below the local topography that minimizes the error between the predicted and observed p-wave arrival times. We then use these locations to initialize an inversion for hypocenters using a centered, scaled version of Newton's method. The centering (subtraction of the mean from the linearized equations) removes the source origin time as an inversion parameter, while scaling normalizes the columns of the Jacobian matrix, thereby reduces it's rank, and improves the problems' conditioning [Gibowicz and Kijko, 1994, Section 4.1]. The uncertainty in the s-wave pick-times are too large to provide additional constraint for locating. The epicentral locations obtained from the inversion are illustrated in Figure 7.

3.5. **Analysis of Icequake Moment.** Seismic moment tensors provide a description of the focal mechanism of icequakes and a measure of their strength. Physical sources like cracks or faults often are modeled as combinations of force-couples using the seismic moment tensor $\mathbf{M}$ which also governs the geometry of the far-field p-wave displacement $\mathbf{u}^P$ [Aki and Richards, 2002, Equation 4.97]. The moment magnitude is characterized by the scalar moment which is defined by the moment norm, $M_0 = \frac{1}{\sqrt{2}}\,||\mathbf{M}||_2$. In practice, M_0 is estimated by contracting the displacement with the p-wave direction $\hat{\mathbf{e}}_p$ at the free-surface and integrating over time [Boatwright, 1980, Equation 5], so that

$$M_0 = \frac{4\pi r\,\Omega}{F_C}\,\frac{\sqrt{\varrho(\mathbf{x})\varrho(\mathbf{x}_0)\alpha(\mathbf{x})\alpha^5(\mathbf{x}_0)}}{\hat{\mathbf{\Gamma}}^{\mathrm{T}}\hat{\mathbf{M}}\hat{\mathbf{\Gamma}}}, \tag{4}$$

Here r is the source-to-receiver distance, Ω is the area under the attenuation-corrected p-wave seismogram, F_C is the free-surface amplification, ϱ is medium density (ice or bedrock), $\mathbf{x}_0$ is the source position, $\mathbf{x}$ is the receiver position, α is p-wave speed, $\hat{\mathbf{\Gamma}}$ is the vector pointing from the source to the receiver, and $\hat{\mathbf{M}}$ is the normalized moment tensor. Physically, M_0 is proportional to either total slip along the crack face or local volume change from crack face opening. We use the volumetric interpretation in this study. Then, the total confined volume change δV at the source region from an icequake is related to the scalar moment of that icequake according to [Richards and Kim, 2005, Equation 1]:

$$M_0 = \delta V\,(\lambda + 2\mu)\,, \tag{5}$$

Elastic parameters are $\lambda \cong 6.5\,\mathrm{GPa}$, $\mu \cong 3.5\,\mathrm{GPa}$, at -16° C [Gammon et al., 1983]. An alternative expression $M_0 = \Delta V\left(\lambda + \frac{2\mu}{3}\right)$ is frequently used in place of Equation 5, where $\Delta V \approx 2\delta V$. However, ΔV gives the volume

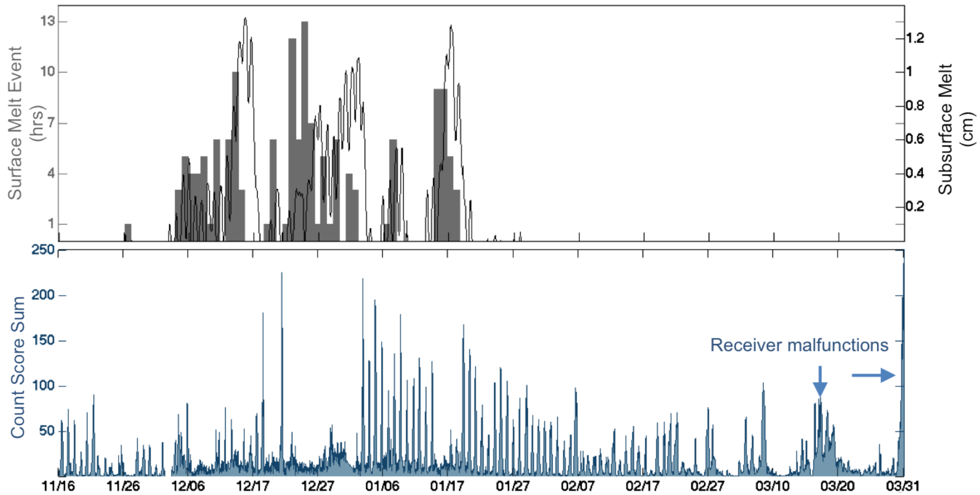

Figure 4. ***Top:*** *Bar plot illustrates hours of active surface melt production, line graph illustrates the depth of the subsurface melt column.* ***Bottom:*** *The net seismicity coincident with modeled melt, summed over each hour. Transition from diurnal to adiurnal seismicity are accompanied by melting events.*

change in stress-free conditions, whereas confinement of buried source prevents the true strain from attaining a stress-free state [Aki and Richards, 2002, Problem 3.8]. We therefore use Equation 5 to compute δV for icequake sources.

4. Interpretations

4.1. **Melt and Seismicity.** The surface and subsurface melt computed from the energy balance model (Section 3.1) are both illustrated in Figure 4 (top). Surface melt was confined to brief, sub-daily events in December and January, with peak melt rates $\leq 1.2\,\mathrm{mm\,hr^{-1}}$. Subsurface melt was also present within the ice column at shallow depths ($\leq 50\,\mathrm{cm}$) both December and January, with and without coincident surface melt. We estimate that a fraction of the water produced in the subsurface over the season ($\cong 1.8\,\mathrm{cm}$) drained through intergranular veins or subsurface cracks, with drainage rates $\leq 0.5\,\mathrm{mm\,hr^{-1}}$. Comparatively, the surface melt was abrupt in timing and we interpret it as a binary process as represented in Figure 6 (top). Figure 4 (bottom) illustrates the total seismicity (Section 3.2) coincident with modeled melt; a non-geophysical train of voltage spikes recorded on two separate receivers biased the noise floor during March and are labeled as malfunctions. For the remainder of observation, both the amplitude and timing of seismicity during melt events is qualitatively distinct from the seismicity measured during periods without melt. When melt is absent, the seismicity is diurnally responsive and minimum emission rates (background rates) are near zero and maximum emission rates consistently occur in early morning hours (Figure 5). During melt events, the signal is less variable or responsive to diurnal forcing, and contains a nonzero background emission rate. Ice speeds observed during melt events show no measurable change, consistent with a glacier frozen to it's bed.

First, we consider the possibility that the diurnal signal is borne from seismic instrumentation noise that would either lead to false STA/LTA triggers or mask waveforms in noise. However, because detections require $2 \leq t \leq 6$ near-simultaneous pick times t for a non-zero count score assignment, we suggest that low SNR are more problematic than false picks. We therefore estimate the statistics for 10^3, 30 sec noise sequences recorded on each receiver from dates uniformly distributed over the observation period and discard any within 30 sec of a known pick time. From these sequences, we observe that the noise is near-Gaussian with diurnal fluctuations in sample variance. We use the array-averaged sample statistics for each hour and compute sample probabilities of both false triggers and missed

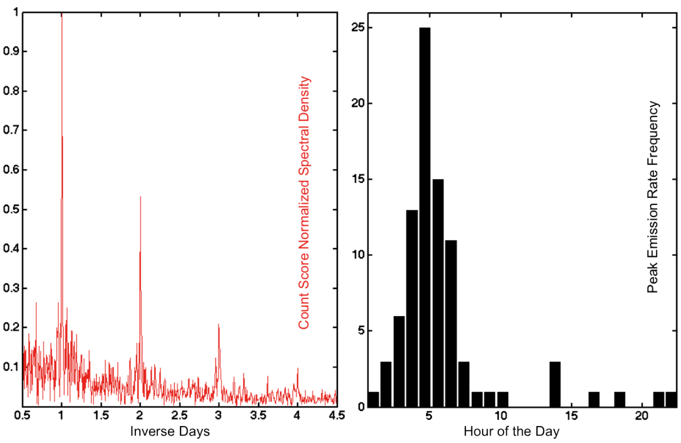

FIGURE 5. ***Left:*** *The amplitude spectra for seismicity from Figure 4 illustrates a strong diurnal component and decaying harmonics.* ***Right:*** *The histogram for times of peak icequake emission observed during diurnal seismic activity. The highest activity occurs during early morning hours.*

signals buried in noise. We conclude that observed seismicity is physical rather than a result diurnal noise, with a 95% confidence level.

We next determine if the seismicity is attributable to the glacier versus the lake ice and consider the signals from particular subsets of the array, or sub-arrays. Our count scoring (Section 3.2) assigns each seismic event a single count score (Equation 1) that is determined by it's observability on each receiver with the event detector. Hence the score is a measure of event size, and the observing-receiver aperture illustrates the general source region. The seismic events observed exclusively on ice-based stations (the ice sub-array) and exclusively on land-based stations (the ground sub-array) are each separable from the net count and provide a measure of the seismicity observed from those regions. Thus these events are of intermediate size. Further, events detected only on the ice sub-array are likely to be glacial icequakes, whereas events detected only on the land array are unlikely to be glacial in origin. Figure 6 (bottom) illustrates the contrast in timing between the ice sub-array versus ground sub-array seismicity. Whereas seismic events observed exclusively on the ice sub-array are active during the melt season, the events observed exclusively on the ground sub-array are active from late January through the remainder of the observation period, with little overlap. This suggests that there are at least two different mechanisms for triggering seismic events of intermediate size. One set triggers glacial icequakes, and the other drives seismicity exterior to the glacier, such as lake ice.

We propose that the diurnally responsive icequake sources that are active without melt include cracking of lake ice (and glacial ice to a lesser extent) through generation of thermal bending moments. These occur in thick sea ice [Bažant, 1992] when thermal stresses near the surface induce bending moments that store significant strain energy. The release of that strain energy can cause large fracture events and result in microseismic emissions that are recorded as icequakes. This is more effective at lengthening large seismogenic cracks in ice compared to thermal diffusion, which is restricted to penetration depths of ~ 10 cm over a daily temperature cycle. Conversely, surface melt apparently triggers seismic events that are not sensitive to diurnal forcing and produces more steady emission of icequakes. We propose the presence of melt creates a heat sink and maintains more uniform ice temperatures, thereby suppressing thermal bending moments and resultant icequakes.

4.2. **Large Icequakes and Multiplet Sources.** We next evaluate the seismicity due to the largest seismic events. In Figure 6 (middle), we compare the ice sub-array seismicity with the seismicity due to events observable on all receivers with unit score. From this comparison, we draw two primary conclusions: first, from the strong coincidence of large seismic events with glacial icequakes, we conclude that the large events are glacial in origin and reject the possibility that they are due to a source exterior to the glacier, such as lake ice. Second, from the timing of melt relative to icequake response, we conclude that these large icequakes are driven by meltwater input. We measure the

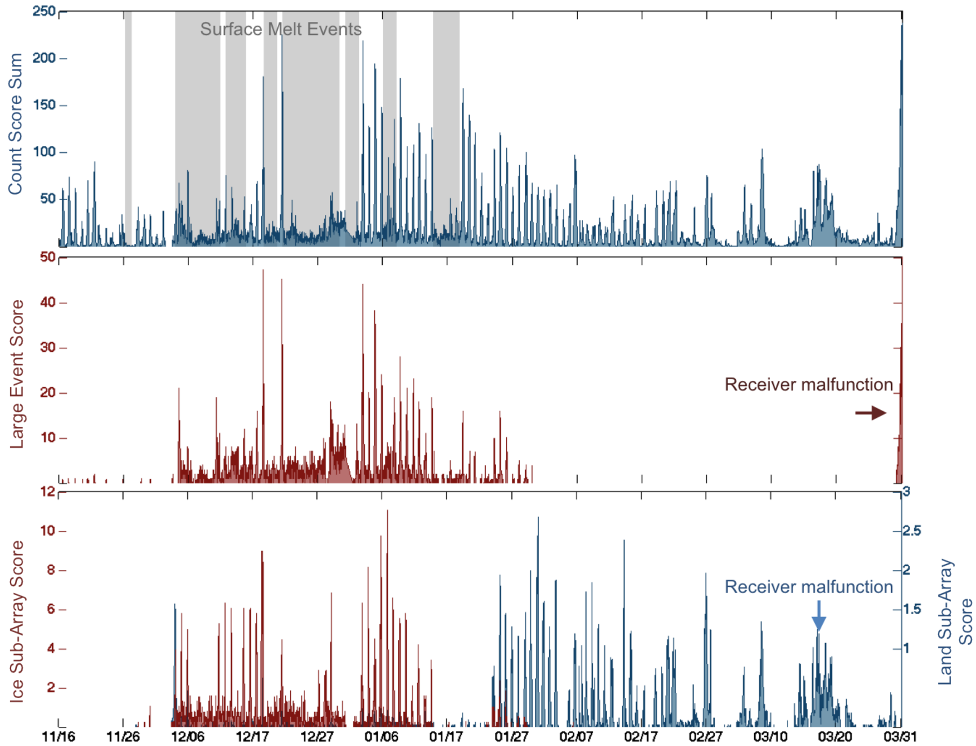

FIGURE 6. ***Top**: The binary occurrence of surface melt (gray) with net seismicity. "On" melt is coincident with non-zero background emission rates and adiurnal seismicity, while "off" melt is coincident near zero background emission rates and diurnal seismicity. **Middle**: The seismicity of the largest icequakes detected, which were recorded by every receiver in the array. These large events are temporally coincident with surface melt. **Bottom**: The seismicity recorded by the ice array (red) compared to the seismicity recorded by the land array (blue). The ice-array seismicity is coincident with both large icequakes (middle) and melt (top), but distinct from the land array seismicity, suggesting that large icequakes are glaciogenic in origin.*

prevalence of melt triggered sources of large icequakes as the number of multiplets coincident with modeled surface melt. Multiplets often result from repeated stress release within the same source region and produce highly correlated record sections within clusters. Therefore, we identify these multiplets with our clustering algorithm (Section 3.3). We run this algorithm over each day of observation in order to build templates from multiplets with short ($\Delta t \leq 24$ hour) activity durations and distinct onset dates (day-matched templates). This clustering reveals 205 distinct populations of multiplets that are composed of 900 individual repeating icequakes. These multiplets are frequently observed during melt events, with the most populous clusters composed of icequakes that occur from early December 2005 through January 2006 (Figure 10, top).

To identify the physical sources of these multiplets, we first search daily images recorded by the camera array for visual events on the glacier corresponding to multiplet observation. We document at most 7 changes to the ice cliff walls or the debris apron at the cliff-base that indicate calving events. We find no further evidence from event detections that precursory activity from calving was seismic as opposed to aseismic. We therefore reject calving as a significant source of seismicity, and next consider icequake source locations. Using our phase pick data set, we apply our inversion scheme (Section 3.4) and assemble a catalog of the corresponding icequake hypocenters. The dominant feature of this catalog is the concentration of epicenters within a "cloud" just west and nearly parallel to the Blood Falls crack (Figure 7). The icequake depths were poorly constrained from the tight elevational coverage of the array

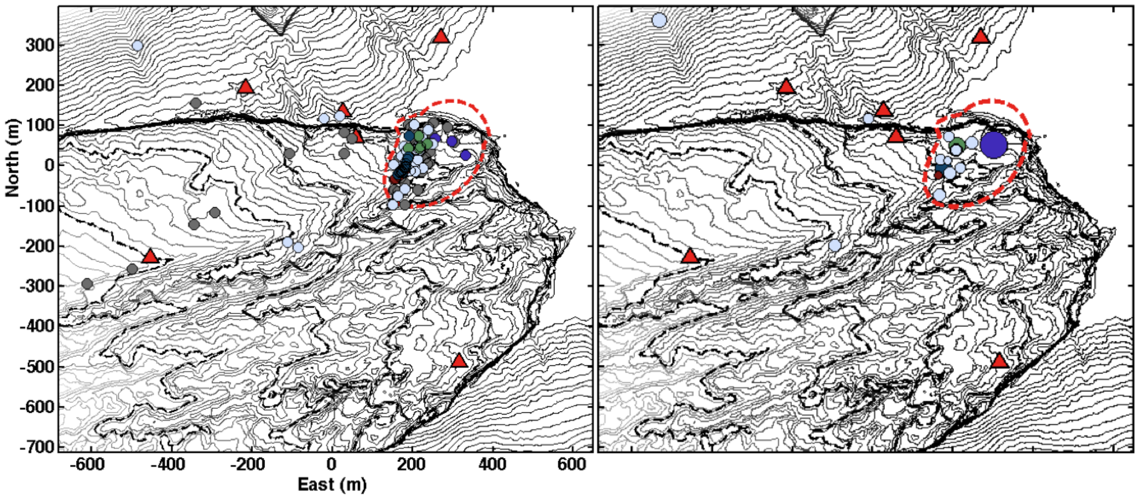

FIGURE 7. ***Left:*** *Icequake epicenters for all located events. The epicenter markers for the most populous four multiplets are distinctly colored, pale blue markers are assigned to the remaining multiplet events, and gray markers are assigned to non-repeating events. The red dashed region at the terminus illustrates the position of the* 95% *confidence region for an icequake source located at the Blood Falls crack tip.* $\sim$ 75% *of located events are within this region during the mid-December to January melt season, suggesting that the crack distribution here is responsible for the observed seismicity. All events were located in December or January.* ***Right:*** *Icequake multiplet centroids. The marker sizes are proportional to the square-root of the cluster population. Each cluster population is identified using template record sections assembled from the stacking the traces of the located events. The most populous cluster is composed of* ≥ 100 *repeating events, most of which were not locatable, but were detectable via clustering.*

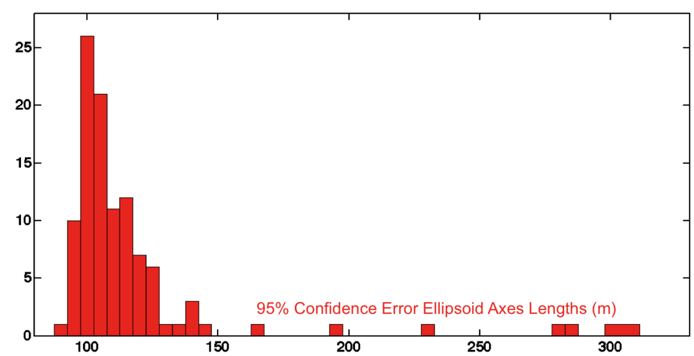

FIGURE 8. *The distribution of location uncertainties for epicentral inversions in Figure 7. Horizontal axis denotes the axes length of* 95% *confidence error ellipsoid in meters.*

we do not interpret them. Of these icequakes, $\sim$ 75% of epicenters are interior to a 95% confidence region centered at the Blood Falls crack tip which we compute from the χ^2 statistic of the weighted residual. We cluster the record sections for these located icequakes and determine that these events comprise 16 multiplet sequences. We then build record-section templates from these events and cluster the remaining catalog using these templates (location-matched templates). We find an additional 211 icequakes that were not located, but match one of the 16 multiplet sequences (Figure 10, middle). Therefore, these events likely originate from the Blood Falls region and occur either during the

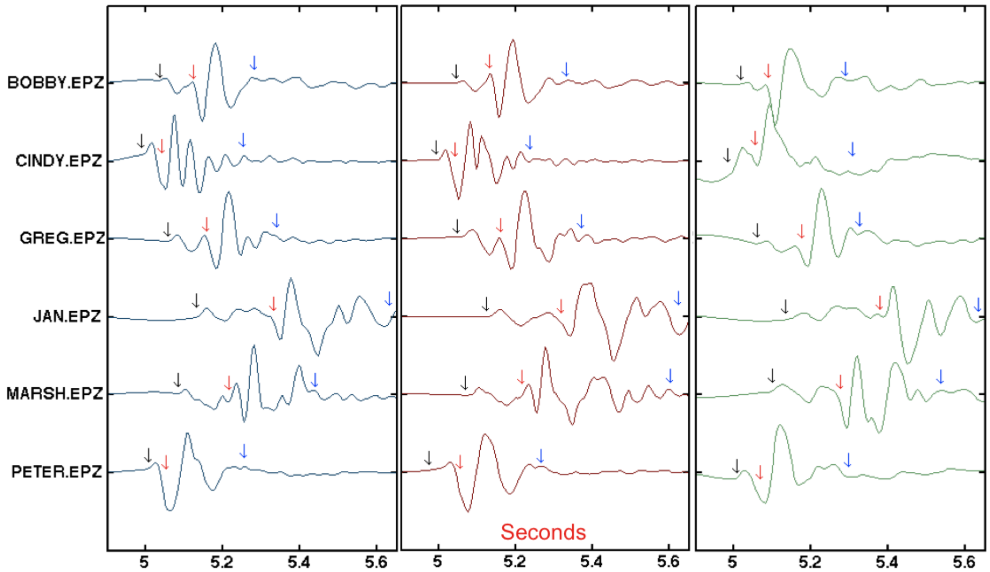

FIGURE 9. *The stacked multiplet waveforms for the vertical channel of the three most populous clusters that were located. Horizontal axes units are in seconds. The trace colors correspond to epicenter marker colors in Figure 7. The black arrows denote* p*-waves, red arrow denotes* s*-waves, and blue arrow the onset of scattered wavefield arrivals. The instrument response has been removed, polarity corrected, and the signals low-pass filtered below* 35 Hz*. For each multiplet population here, the first* p*-wave upward at all azimuths, consistent with a dilatational source.*

melt episodes or soon thereafter (Figure 10, bottom).

Since many locations are tens of meters upstream and parallel to the major crack axis but each absolute location is only constrained at the 95% level within a relatively large region (Figure 8), we suggest an unknown systematic error may also produce the inverted epicenters. Such sources of error are feasible, as waveforms recorded at CINDY often do display confusing low amplitude ripples prior to a more obvious impulsive arrival, and the channel noise on PETER and MARSHA did have higher amplitudes relative to the waveforms. We therefore forward model 0.008 sec early pick times on station CINDY to simulate picks on acausal precursors from impulsive arrivals, and 0.008 sec late pick times on PETER and MARSHA to simulate post-arrival picking due to signals being below noise level. We find that inverted epicenters with erroneous picks lead to observed locations for a Blood Falls source consistent with what we observe.

4.3. **First Motions and Focal Mechanisms.** We stack the record sections from the located icequakes using the three most populous multiplet sequences to obtain a representative signal from the source region. Waveforms for these multiplet sequences have common traits of microseismic events: arrivals are impulsive, coherence between receivers is low, and coda waves dominate the latter portion of the wave train. This is consistent with a short duration source-time function and strong scattering environment [Oye et al., 2005]. The polarity of the direct p-wave for these stacked record sections in Figure 9 is up, and away from the source location at all receivers. This uniform p-wave polarity is consistent with a source composed of volumetric or isotropic focal mechanisms [Walter et al., 2008]. One physically plausible source that will generate these motions is the tensile crack [Aki and Richards, 1980]. Because the icequake locations are upstream of the current crack, we propose that we are observing the formation of the seep crack tip as it advects downstream and matures into a deeper feature. The ice flow pattern develops a simple shear stress pattern that leads to en echelon crevasses forming 45 degrees to the flow. We propose that the seismicity near the upstream crack impy that this crack is in its development stage and is opening at a faster rate of strain. As the ice is advected through this stress pattern, the crack-opening stresses are reduced, but the crack remains open

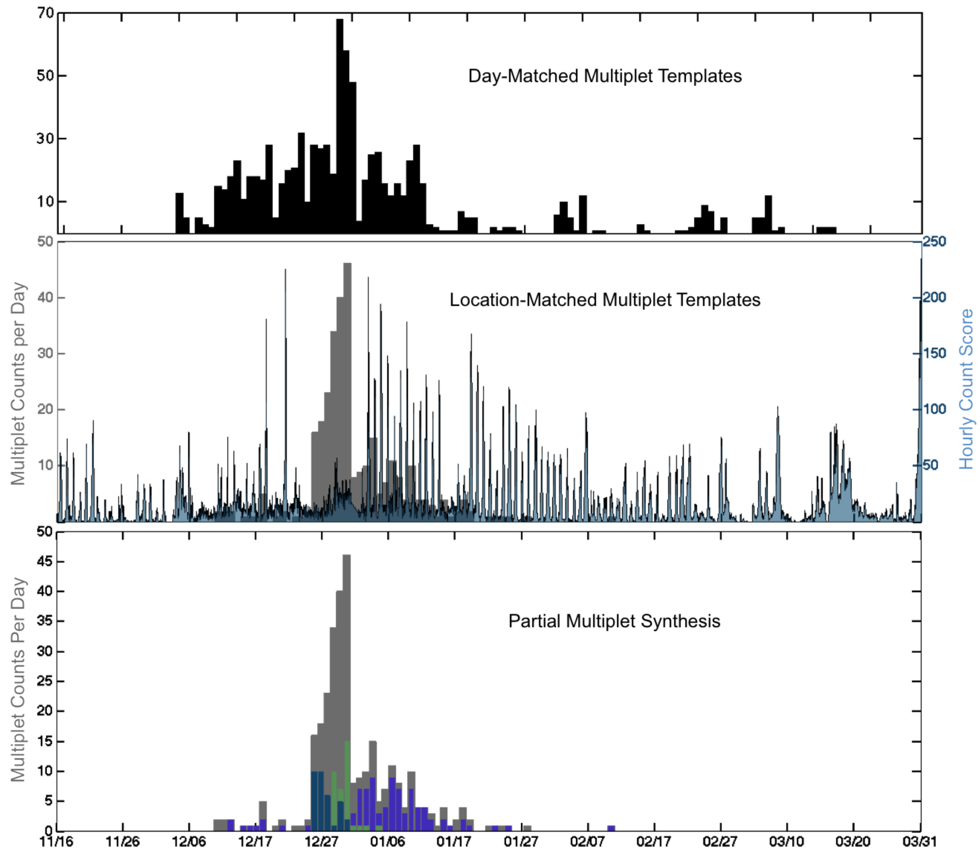

FIGURE 10. ***Top**: Frequency of multiplets detected per day, using the template-stacks from the entire observation period. The peak activity occurs during late December during melt episodes. **Middle**: A comparison between the total seismicity (blue), and the frequency of multiplet events (gray bar) found using record section templates taken from located icequakes (location-matched multiplet templates). Repeating icequakes are activated during the mid-December period, which is characterized by large events and adiurnal seismicity. **Bottom**: A partial synthesis of the location-matched multiplet count, using multiplets detected from the events located in Figure 7; bar colors correspond to epicentral marker colors. Because relative source locations are constrained by mutual correlation, this implies seismicity observed during this period is largely due to repeating icequakes near Blood Falls.*

allowing the flow from the Blood Falls seep. The downstream crack face forms a principle plane where tensile stresses are minimized.

A second kind of source that is capable of producing the observed first motions is the volumetric expansion of a pressurized source of brine at depth, analogous to what is observed in volcanic or geothermal systems [Thelen et al., 2010]. The surface channels of Taylor carry meltwater off of the glacier and into Lake Bonney, thereby unloading the glacial substrate. Peak melt rates of $1.2\,\mathrm{mm\,hr^{-1}}$ over the glacier surface produce spatially-averaged peak unloading rates of $\dot{m}\rho_W g \cong 12\,\mathrm{Pa\,hr^{-1}}$, where $\dot{m}$ is the melt rate in dimensions of length per time per unit area, ρ_W is water density, and g is gravitational acceleration. Johnston et al. [2005] report melt rates in the channels to be 4.5 times that of measured melt rates on the flat ice surface, giving an upper bound for the peak unloading rate of $\dot{m}\rho_W g \cong 54\,\mathrm{Pa\,hr^{-1}}$. We compute comparable peak unloading rates of order $10\,\mathrm{Pa\,hr^{-1}}$ from atmospheric tides

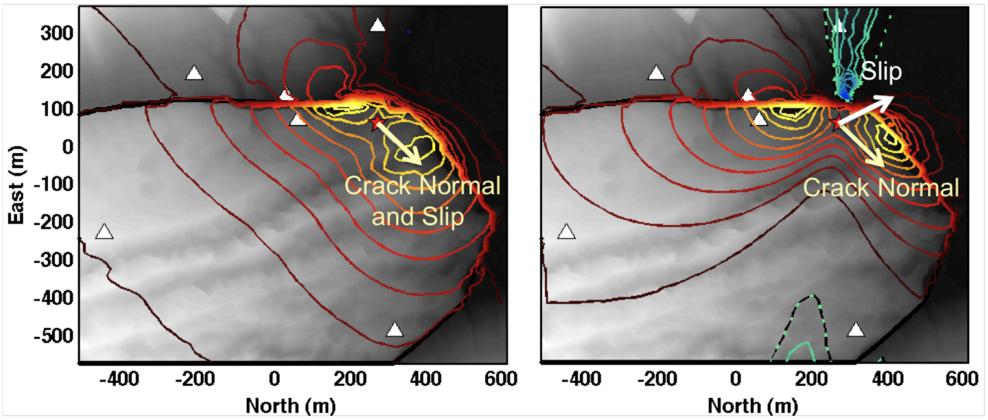

FIGURE 11. ***Left:*** *Contour lines of ground displacement computed from a model of p-wave motion produced from the impulsive opening of a unit-area mode I crack at the center of Blood Falls. The warm colors are indicative of positive polarity.* ***Right:*** *A model of the p-wave ground displacement produced by a mixed mode crack, when the crack face normal and slip direction are within* 71° *of each other. The cool colors are indicative of negative polarity.*

in the Dry Valleys during December through January. We therefore consider the tensile crack model more likely, because the alternative requires the brine source to respond changes in overburden comparable to that produced by atmospheric tides. Our estimates do not consider the effect of pressure gradients caused by changes in ice surface topography from melting, because the energy balance model implemented here is one-dimensional. A more focused seismic study is necessary to assess the possibility of triggering deeper sources from changes to surface loading gradients.

While pure tensile cracking is sufficient for producing compressive p-wave displacements at the receiver locations, it is not necessary. A seismic source composed of modes of fracture in addition to mode I can also produce compressive first arrivals at the six receiver locations. To bound the possible modes leading to the observed polarities, we forward model the p-wave surface displacement resulting from fracture source of unit area, localized at the Blood Falls crack tip. We first compute motions using a description for whole space [Aki and Richards, 2002, Equation 4.97] and a suite of crack face displacement vectors that combine tensile with mode II (slipping) and mode III (tearing) cracking. To estimate the surface motion at each receiver, we then correct for ice-to-ground refraction, surface amplification, and p-wave inclination. Some results of this modeling are illustrated in Figure 11. Crack face displacements oriented more than 68° from the crack face normal result in insufficient tensile cracking that produces downward first motions at receivers, inconsistent with observations. This implies that tensile cracking must account for at least 66% of the moment tensor norm (scalar moment), regardless of the possibility for other fracture modes.

We propose a physical model for melt triggered seismicity that produces the observed compressive first motions as follows. In this model, surface and subsurface melt produced during the December-January season flows down-gradient toward the Blood Falls seep as input into the crack system. Any channel down-cutting that occurs englacially as proposed in temperate glaciers [Fountain and Walder, 1999] would then increase the stress intensity factor of the crack. Once melt production abates, inflow rates decrease, and englacial water at depth freezes quickly where the ice is cold (-17°C). However, some liquid water may persist at depth on wetted ice or rock surfaces as a thin film. The thermomolecular forces responsible for flow within the films have a net body-force equivalent that is proportional to the film-equivalent ice mass [Dash et al., 2006]. This proposed process can generate $\sim 2\,$MPa stresses responsible for frost-heave in frozen ground [Murton et al., 2006]. We therefore suggest that the presence of this crack allows a persistent surface pathway for the Blood Falls source by acting as both a catchment for meltwater and cite for fracture by ice segregation.

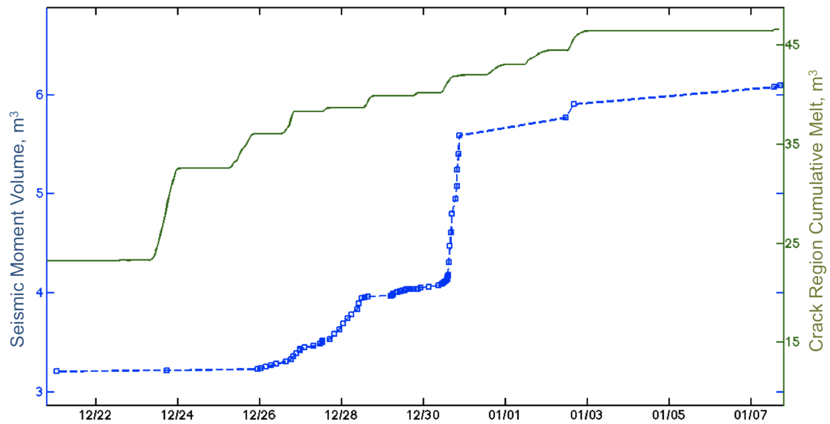

Figure 12. *The cumulative modeled melt volume over the Blood Falls crack region is compared with the volumetric increase at the source region. The melt includes contributions from both the surface and subsurface, and the volume increase at the source region is computed from Equation 6. Markers on source-volume plot indicate volume changes for individual ice quakes.*

4.4. **Moment and Volume Change.** To estimate the volume change at the source region over the melt season, we first compute M_0 for icequakes interior to the 95% confidence interval at the tip of the Blood Falls crack. We can only use station JAN to compute moment with Equation 4 within the confidence we require, however. This is because the differential arrival times between p- and s-waves are too small or uncertain, relative to the sample interval, to provide adequate measurements of $\Omega(x, 0)$. There are additional sources of uncertainty in our application of Equation 4 that are difficult to quantify; for example, the quality factors that we use for attenuation correction ($\sim 10^1 - 10^2$) are not well known, the p-wave pulse may include scattered arrivals that we unintentionally integrate with $\Omega(x, 0)$, and $\hat{\mathbf{\Gamma}}$, and F_C depend on uncertain hypocentral depths. We therefore compute icequake magnitudes using the moment-magnitude scale $M_w = \frac{2}{3}\left(\log_{10} M_0 - 9.1\right)$ [Kanamori, 1977] to evaluate the reasonability of our M_0 estimates. We find that $-0.70 \leq M_w \leq +0.31$. Compared with icequakes on alpine glaciers of comparable thickness, these magnitudes are between that of crevassing and basal stick-slip events (Steve Malone, personal communication), and similar to those observed from microseismicity in mines (e.g., Gibowicz and Kijko [1994]). We conclude our measurements of scalar moment are within expectation. Finally, to estimate volume change at the source region, we assume the icequakes from the crack region have similar mechanisms and sum the cumulative scalar moment with Equations 4 and 5:

$$(\lambda + 2\mu)\, \Delta V = \sum_k M_0^{(k)} \tag{6}$$

From Equation 6, we compute a source volume change of $\cong 6\,\mathrm{m}^3$ at the source region. When we average this volume over an 80 m crack at 15 m deep, we estimate a cumulative crack opening displacement of 5 mm. The melt rates modeled during this time exceed a cumulative water volume of ≈ 4 mm per unit area, and the required source-volume increase computed from Equation 6 (Figure 12). The relatively small displacements may explain why no obvious GPS speed-up is observed during the melt season in spite of icequake activity.

5. Synthesis and Future Work

Our goal in conducting this study was to determine the response characteristics of a dry, polar glacier during the transition into a melt season when meltwater influences the deformation of the ice. Our methodology consists of modeling surface melt using an energy balance model, and comparing this to passive seismic data that we process using array-based analyses. From our estimate of surface melt and interpretation of the icequake observables, we make three primary conclusions: first, very little meltwater initiates a mode of seismicity distinct from the diurnally responsive, dry, cold mode. The melt-driven mode is composed of comparatively few but large energy icequakes, with little response to diurnal forcing. Second, the response time at Taylor Glacier is effectively immediate, with most large icequakes triggered nearby the Blood Falls existing cracks. Third, the first p-wave motions from sources indigenous to the fractured region are consistent with opening cracks. One implication of water driven fracture in cold ice is that surface melt may reach the sub-freezing bed, and hence allow brief input of heat and mass to the cold basal interface. This does not seem to require the existence of persistent englacial water that exists in temperate ice, and has been observed in the Canadian arctic [Boon and Sharp, 2003]. The velocities as determined from GPS show no speedup above measurement noise; hence if meltwater does penetrate to the bed, no basal sliding likely takes place. A second implication is that the re-freezing of surface melt in deep cracks may trigger sufficient crack tip propagation to allow persistent communication to the pressurized Blood Falls brine source at depth. The crack propagation is not likely to be driven by hydrofracturing that results from high overburden pressures in a water-filled crack as discussed elsewhere, however. We propose that once the crack formed and enabled brine to escape, it acted as a catchment during melt seasons and induced further fracture through possible downcutting and refreezing, thereby allowing the crack to persist. In wetter conditions, other surface cracks may catch comparable water and create additional pathways to the surface. Thus, the singularity of the release point for the brine may be due to the low melt rate at Taylor. Thus, broader impacts of this study may include providing the micro-biology community an opportunity to assess the role of surface controls on the brine release episodes.

We cannot reject the possibility that a fault system exists beneath the bedrock near Blood Falls. Such a fault feature may act as a conduit for the Blood Falls seep and induce high tensile stresses at the glacier surface through fault movement, thereby promoting surface fracture and englacial hydrological communication.

Appendix A. Unsupervised Clustering of Record Sections

Define a Hilbert space $\mathcal{H}$ equipped with an inner product $\langle \bullet, \bullet \rangle$ whose elements are $3N$ channel record sections $\mathbf{v}(t)$. Suppose that $\mathbf{u}_k(t)$, $k = 1, \ldots, n, \ldots, M$, are record sections as defined by Equation 2, that give samples of ground motion from M icequakes. Consider a set $S \subset \mathcal{H}$ according to the membership criteria:

$$S = \{\mathbf{v}(t) : \langle \mathbf{v}(t), \hat{\mathbf{u}}_n(t) \rangle \geq \rho_0 \, ||\mathbf{v}(t)||\}\,, \tag{7}$$

Equation 7 defines a higher dimensional convex cone whose vertex is parallel to $\hat{\mathbf{u}}_n(t)$ and represents the set of all record sections that belong to a multiplet [Stark and Yang, 1998, p. 113]. Seismic clustering methods often implicitly use sets of this form [Lees, 1998]. Populating set S requires prescribing $\hat{\mathbf{u}}_n(t)$, unfortunately. We define a cluster as a smaller convex set using a more restrictive membership criteria:

$$S_L = \{\mathbf{v}(t) : \langle \mathbf{v}(t), \hat{\mathbf{u}}_k(t) \rangle \geq \rho_0 \, ||\mathbf{v}(t)||\}\,, \quad \forall\, k \in [1, L] \tag{8}$$

where $L \leq M$. Elements of S_L correlate above ρ_0 with every record section $\mathbf{u}_k(t)$, $k = 1, \ldots, n, \ldots, L$, so that $S_L \subseteq S$. It also represents record sections produced by a multiplet, but the characteristic ground motion is provided by L observations, rather than one. Hence, clustering record sections into sets defined by Equation 8 requires high *mutual* correlation between elements. We implement this requirement as follows. Suppose we detect M icequakes on a given day and record M corresponding record sections. From Equation 3, we define an upper-triangular matrix $\boldsymbol{\rho}$ whose elements ρ_{ij} provide the $\frac{1}{2}\left(M^2 - M\right)$ normalized correlation coefficients between record sections:

$$\rho_{ij} = \max_{\tau} \frac{\langle \mathbf{u}_i(t), \mathbf{u}_j(t+\tau) \rangle_F}{||\mathbf{u}_i(t)||_F \, ||\mathbf{u}_j(t)||_F}, \quad i < j \tag{9}$$

Suppose now that a subset of $L \leq M$ record sections with indices $\gamma \subseteq \{1, \ldots, L\}$ cross-correlate above ρ_0 with a particular record section $\mathbf{u}_n(t)$, so that $\rho_{n\gamma} \geq \rho_0 \;\forall\; \gamma$. This does not guarantee that $\mathbf{u}_\gamma(t) \in S_L \;\forall\; \gamma$. We therefore check all entries of $\boldsymbol{\rho}$ whose indices are derived from pair-wise combinations of γ as power sets. For example, if $\rho_{1\gamma} \geq \rho_0 \;\forall\; \gamma = \{2, 3, 7\}$, then $\mathbf{u}_\gamma(t) \in S_L \;\forall\; \gamma$ only if ρ_{23}, ρ_{27}, and ρ_{37} each exceed ρ_0 as well. If this condition holds, we define $S_L = \{\mathbf{v}(t) : \langle \mathbf{v}(t), \hat{\mathbf{u}}_k(t) \rangle \geq \rho_0 \, ||\mathbf{v}(t)||\}, \forall\, k \in [1, 2, 3, 7]$ as the cluster for a multiplet event.

In general, we identify the clusters from Equation 9 for each day, and aggregate them over the total observation period by computing $\boldsymbol{\rho}$. To populate the final clusters that are plotted in Figure 10 (top), we check mutual correlation between all elements that satisfy $\rho_{ij} \geq \rho_0$ as for daily observations. We obtain a representation of a each cluster by coherently aligning the elements to sub-sample precision and summing (stacking) them linearly. Because S_L is convex, any linear combination of record sections with non-negative weights is also contained in S_L. Other weighting schemes for stacking are useful but depend on the performance measure applied to the record section output. A subspace method for obtaining a multiplet representation is thoroughly described elsewhere [Harris, 1989].

Appendix B. Acknowledgements

We extend thanks to Ken Creager and Ian Joughin who provided input concerning the seismic and glaciological aspects of the work. We thank UNAVCO, IRIS-PASSCAL, and Raytheon for providing instrumentation and logistical support. We thank the members of the Blood Falls field team Matt Szundy, Erin Whorton, Hassan Basajic, Michelle Koutnik and Thomas Nylen that assisted in the collection of the seismic data used in this work. This work was supported by NSF grant 0230338.

References

Keiti Aki and Paul G. Richards. *Quantitative Seismology.* W.H. Freeman and Company, San Francisco, CA, USA, 1980.

Keiti Aki and Paul G. Richards. *Quantitative Seismology.* University Science Books, Sausalito, CA, USA, 2nd edition, 2002.

Zdeněk P. Bažant. Large Scale Thermal Bending of Sea Ice Plates. *Journal of Geophysical Research*, 97(C11): 17739–17751, 1992.

John Boatwright. Spectral Theory for Circular Sesimic Sources; Simple Estimates of Source Dimension, Dynamic Stress Drop, and Radiated Seismic Energy. *Bulletin of the Seismological Society of America*, 70(1):1–27, 1980.

Sarah Boon and Martin. Sharp. The Role of Hydrologically-Driven Ice Fracture in Drainage System Evolution on an Arctic Glacier. *Geophysical Research Letters*, 30(1916), 2003. doi: 10.1029/2003GL018034.

Richard E. Brandt and Stephen Warren. Solar-Heating Rates and Temperature Profiles in Antarctic Snow and Ice. *Journal of Glaciology*, 39(131):99–110, 1993.

GKC Clarke. Subglacial Processes. *Annual Review Of Earth and Planetary Sciences*, 33(128):247–276, 2005. doi: 10.1146/annurev.earth.33.092203.122621.

Sarah B. Das, Ian Joughin, Mark D. Behn, Ian M. Howat, Matt A. King, Dan Lizarralde, and Maya P. Bhatia. Fracture propagation to the base of the greenland ice sheet during supraglacial lake drainage. *Science*, 320(5877): 778–781, May 2008. doi: 10.1126/science.1153360.

J.G. Dash, A.W. Rempel, and J. S. Wettlaufer. The Physics of Premelted Ice and its Geophysical Consequences. *Reviews of Modern Physics*, 78(3):695–741, 2006. doi: 10.1103/RevModPhys.78.695.

N. Deichmann, J. Ansorge, F. Scherbaum, A. Aschwanden, F. Bernardi, and G.H. Gudmundsson. Evidence for deep icequakes in an Alpine glacier. *Annals of Glaciology*, pages 85–90, 2000.

Andrew G Fountain and Joseph S. Walder. Water Flow through Temperate Glaciers. *Reviews of Geophysics*, 36(3): 299–328, 1999.

Andrew G. Fountain, Thomas H. Nylen, Karen Lewis MacClune, and Gayle L. Dana. Glacier Mass Balances (1993-2001), Taylor Valley, McMurdo Dry Valleys, Antarctica. *Journal of Glaciology*, 52(178):451–462, 2006.

P.H. Gammon, H. Kiefte, M.J Clouter, and W.W. Denner. Elastic-Constants of Artificial and Natural Ice Samples by Brillouin Spectroscopy. *Journal of Glaciology*, 29(103):433–460, 1983.

Steven J. Gibbons and Frode Ringdal. The Detection of Low Magnitude Seismic Events using Array Based Waveform Correlation. *Geophysical Journal International*, 165(1):149–166, 2006.

Slawomir Jerzy Gibowicz and Andrzej Kijko. *An Introduction to Mining Seismology.* Academic Press, San Diego, CA, USA, 1994.

David B. Harris. Characterizing Source Regions with Signal Subspace Methods: Theory and Computational Methods. Technical Report UCID-21848, Lawrence Livermore National Laboratory, December 1989.

David B. Harris. A Waveform Correlation Method for Identifying Quarry Explosions. *Bulletin of the Seismological Society of America*, 81(6):2395–2418, December 1991.

David B. Harris. Subspace Detectors: Theory. Technical Report UCRL-TR-222758, Lawrence Livermore National Laboratory, July 2006a.

David B. Harris. Subspace Detectors: Efficient Implementation. Technical Report UCRL-TR-223177, Lawrence Livermore National Laboratory, July 2006b.

Matt J. Hoffman. *Spatial and Temporal Variability of Glacier Melt in the McMurdo Dry Valleys, Antarctica*. PhD thesis, Portland State University, 2011.

Matthew J. Hoffman, Andrew G. Fountain, and Glen E. Liston. Surface energy balance and melt thresholds over 11 years at Taylor Glacier, Antarctica. *Journal of Geophysical Research*, 113:F04014, 2008. doi: 10.1029/2008JF001029.

Federation of Digital Seismograph Networks: Standard for the Exchange of Earthquake Data, Reference Manual, SEED Format Version 2.4. Incorporated Research Institutions for Seismology, 2.4 edition, May 2010. URL http://www.iris.edu/manuals/. 141–159.

Robin R. Johnston, Andrew G. Fountain, and Thomas H. Nylen. The origin of channels on lower Taylor Glacier, McMurdo Dry Valleys, Antarctica, and their implication for water runoff. *Annals of Glaciology*, 40:1–7, 2005.

Hiroo Kanamori. The Energy Release in Great Earthquakes. *Journal of Geophysical Research*, 82(20):2981–2987, 1977. doi: 10.1029/JB082i020p02981.

J. L. Kavanaugh and K.M. Cuffey. Dynamics and mass balance of Taylor Glacier, Antarctica: 2. Force balance and longitudinal coupling. *Journal of Geophysical Research*, 114:F04011, 2009. doi: 10.1029/2009JF001329.

Andrzej Kijko and M. Sciocatti. Optimal Spatial Distribution of Seismic Stations in Mines. *International Journal of Rock Mechanics and Mining Sciences*, 32(6):607–615, September 1995. doi: 10.1016/0148-9062(94)00052-5.

Jonathon M. Lees. Multiplet Analysis at Coso Geothermal. *Bulletin of the Seismological Society of America*, 88(5): 1127–1143, October 1998.

Glen E. Liston and Kelly Elder. A Distributed Snow-Evolution Modeling System (SnowModel). *Journal of Hydrometeorology*, 7(6):1259–1276, 2006.

Glen E. Liston, Jan-Gunnar Winther, Oddbjrn Bruland, Hallgeir Elvehy, and Knut Sand. Below-Surface Ice Melt on the Coastal Antarctic Ice Sheet. *Journal of Glaciology*, 45(150):273–285, 1999.

Jill A. Mikucki, Ann Pearson, David T. Johnston, Alexandra V. Turchyn, James Farquar, Daniel P. Schrag, Ariel D. Anbar, John C. Priscu, and Peter A. Lee. A Contempary Microbially Maintained Subglacial Ferrous Ocean. *Science*, 324:397–400, 2009.

Julian B. Murton, Rorik Peterson, and Jean-Claude Ozouf. Bedrock Fracture by Ice Segregation in Cold Regions. *Science*, 314(5802):1127–1129, 2006. doi: 10.1126/science.1132127.

Volker Oye, Hilmar Bungum, and Michael Roth. Source Parameters and Scaling Relations for Mining-Related Seismicity within the Pyhasalmi Ore Mine, Finland. *Bulletin of the Seismological Society of America*, 95(3): 1011–1026, 2005. doi: 10.1785/0120040170.

Paul G. Richards and Won-Young Kim. Equivalent Volume Sources for Explosions at Depth: Theory and Observations. *Bulletin of the Seismological Society of America*, 95(186):401–407, 2005. doi: 10.1785/0120040034.

P.F. Roux, F. Walter, P. Riesen, S. Sugiyama, and M. Funk. Observation of Surface Seismic Activity Changes of an Alpine Glacier during a Glacier-Dammed Lake Outburst. *Journal of Geophysical Research*, 115:F03014, 2010. doi: 10.1029/2009JF001535.

Pierre-Francois Roux, David Marsan, Jean-Philippe Metaxian, Gareth O'Brien, and Luc Moreau. Microseismic activity within a serac zone in an alpine glacier (Glacier d'Argentiere, Mont Blanc, France). *Journal of Glaciology*, 54(184):157–168, 2008.

D. Samyn and S. J. Fitzsimons. Dynamic implications of discontinuous recrystallization in cold basal ice: Taylor Glacier, Antarctica. *Journal of Geophysical Research*, 113:F03S90, 2008. doi: 10.1029/2006JF000600.

David E. Shean, James W. Head III, and David R. Marchant. Shallow seismic surveys and ice thickness estimates of Mullins Valley debris-covered glacier, McMurdo Dry Valleys, Antarctica. *Antarctic Science*, 19(4):485–496, 2007.

Roel Snieder and Mark Vrijlandt. Constraining the Source Separation with Coda Wave Interferometry: Theory and Application to Earthquake Doublets in the Hayward Fault, California. *Journal of Geophysical Research*, 110: B04301, April 2005. doi: 10.1029/2004JB003317.

Henry Stark and Yongyi Yang. *Vector Space Projections.* Wiley John and Sons, Incorporated, New York, NY, 1998.

Weston Thelen, Mike West, and Sergey Senyukov. Seismic Characterization of the Fall 2007 Eruptive Sequence at Bezymianny Volcano, Russia. *Journal of Volcanology and Geothermal Research*, 194(4):201–213, 2010.

Fabian Walter, Nicholas Deichmann, and Martin Funk. Basal icequakes during changing subglacial water pressures beneath Gornergletscher, Switzerland. *Journal of Glaciology*, 54(186):511–521, 2008.

Fabian Walter, Douglas S. Dreger, John F. Clinton, Nicholas Deichmann, and Martin Funk. Evidence for near-horizontal tensile faulting at the base of Gornergletscher, a Swiss Alpine Glacier. *Bulletin of the Seismological Society of America*, 100(2):458–472, 2010. doi: 10.1785/0120090083.

C.S. Weaver and S.D. Malone. Seismic Evidence for Discrete Glacier Motion at the Rock-Ice Interface. *Journal of Glaciology*, 23(89):171–184, 1979.